

# A simultaneous maximum likelihood approach for galaxy-galaxy lensing and cluster lens reconstruction

Bernhard Geiger<sup>1,2</sup> and Peter Schneider<sup>1</sup>

<sup>1</sup>*Max-Planck-Institut für Astrophysik, Karl-Schwarzschild-Straße 1, 85740 Garching bei München, Germany*

<sup>2</sup>*Institut d’Astrophysique de Paris, 98bis Boulevard Arago, 75014 Paris, France*

Submitted 1998 April 21

## ABSTRACT

In a previous paper we investigated means for constraining the mass distribution of cluster galaxies by weak lensing. We concluded that a comprehensive method should treat the lensing effects of individual cluster galaxies and those resulting from a general cluster component simultaneously. To this end we now develop a non-parametric maximum likelihood cluster reconstruction algorithm that can implicitly take into account the presence of cluster galaxies. The method includes an entropy-like regularization prescription and directly uses the ellipticities of individual source galaxy images as observables rather than relying on an averaged ellipticity field. The mass distribution of cluster galaxies is described by parametrized models. For each set of galaxy parameters the cluster reconstruction algorithm allows to determine the best representation of the global underlying cluster component that is consistent with the presence of the cluster galaxies and the observed image ellipticities of background galaxies. Tests with simulations yielded convincing and robust results.

We applied the method to a WFPC2 image of the cluster Cl0939+4713 and obtained a detection of the lensing effects of luminous elliptical cluster galaxies. We consider this application as a successful test of our technique. However, the small size of the image we analysed does not yet allow to draw strong conclusions regarding the mass distribution of cluster galaxies.

**Key words:** galaxies: clusters: general – galaxies: clusters: individual: Cl0939+4713 – galaxies: haloes – dark matter – gravitational lensing.

## 1 INTRODUCTION

Weak gravitational lensing was suggested by Tyson et al. (1984) as a means to obtain information on the mass distribution of galaxies at large radial distances. The first detection of weak distortions of the images of background galaxies generated by the tidal gravitational field of intervening galaxies was reported by Brainerd, Blandford & Smail (1996). Griffiths et al. (1996) studied the galaxy-galaxy lensing effects in the *Medium Deep Survey*, and Dell’Antonio & Tyson (1996) and Hudson et al. (1997) analysed the *Hubble Deep Field*. Natarajan et al. (1997) detected the weak lensing effects induced by cluster galaxies in a mosaic of HST-images of the cluster AC114.

In this paper we continue our discussion of methods to constrain the mass distribution of cluster galaxies from weak lensing presented in Geiger & Schneider (1998, hereafter referred to as Paper I). For the maximum likelihood method described in that paper we first obtained a reconstruction of the cluster mass distribution using ‘conventional’ techniques that rely on the inversion of an integral equation.

Then we added parametrized models for the mass distribution of galaxies to the cluster component and applied empirical mass subtraction prescriptions to keep the total mass of the system constant. This approach proved to be workable in the outskirts of clusters where the surface mass density is low. In the non-linear lensing regime in the cluster centre, however, the result turned out to be sensitive to the details of the mass reconstruction and subtraction procedures. For values of the galaxy model parameters that imply a very large fraction of the total mass attributed to galaxies, conceptual problems arise regardless of the (non-)linearity of the lensing effects or the distance from the cluster centre.

In order to overcome these problems we decided to extend the maximum likelihood approach to the problem of determining the mass distribution of the cluster component. This allows to include prior information on the presence of the cluster galaxies directly into the cluster reconstruction procedure. We follow the work of Bartelmann et al. (1996) and use the two-dimensional gravitational potential as the fundamental physical quantity describing the properties of the cluster lens. Likelihood methods for cluster reconstruc-

tion from weak lensing were also described by Squires & Kaiser (1996) and Bridle et al. (1998). These methods use a grid of averaged image ellipticities of background galaxies as observational input. However, the averaging procedure already destroys the information on galaxy scales that we are interested in and therefore we are obliged to use the ellipticities of individual source galaxy images directly as observables. Such an approach for cluster reconstruction was investigated in detail by Seitz, Schneider & Bartelmann (1998), and some elements of the technical implementation of our method are similar to their study.

In Section 2 we describe the combined method for cluster lens reconstruction and galaxy-galaxy lensing that we have developed. The reliability of the method is confirmed by an application to simulated observations presented in Section 3. In Section 4 we use our techniques to analyse a WFPC2 image of the cluster Cl0939+4713, which yields a detection of the lensing effects induced by elliptical cluster galaxies. Section 5 concludes the paper with a discussion of the results.

## 2 METHOD

We continue to use the concepts and definitions introduced in Paper I. In general the symbols for the surface mass density, the shear, and the lensing potential should be understood as referring to (hypothetical) sources located at infinite redshift. For simplicity we omit the  $\infty$ -subscript for the relevant quantities in this paper if additional subscripts are present.

### 2.1 Description of the cluster component

The lensing properties of the cluster component are described by the dimensionless scalar potential  $\psi_\infty$ . The surface mass density  $\kappa_C$  and the shear  $\gamma_C = \gamma_{1C} + i\gamma_{2C}$  are combinations of second derivatives of this potential:

$$\kappa_C = \frac{1}{2}(\psi_{,11} + \psi_{,22}), \quad \gamma_{1C} = \frac{1}{2}(\psi_{,11} - \psi_{,22}), \quad \gamma_{2C} = \psi_{,12}.$$

In practice, we specify the potential  $\psi_{\alpha\beta}$  on a  $(n+2) \times (n+2)$  grid ( $\alpha, \beta = 0, \dots, n+1$ ), and calculate the cluster contribution to the surface mass density  $\kappa_{C\alpha\beta}$  and the shear  $\gamma_{C\alpha\beta} = \gamma_{1C\alpha\beta} + i\gamma_{2C\alpha\beta}$  on a  $n \times n$  grid ( $\alpha, \beta = 1, \dots, n$ ), using discrete versions of the second derivatives:

$$\begin{aligned} \kappa_{C\alpha\beta} &= \frac{1}{2}(\psi_{\alpha+1\beta} + \psi_{\alpha-1\beta} + \psi_{\alpha\beta+1} + \psi_{\alpha\beta-1} - 4\psi_{\alpha\beta}), \\ \gamma_{1C\alpha\beta} &= \frac{1}{2}(\psi_{\alpha+1\beta} + \psi_{\alpha-1\beta} - \psi_{\alpha\beta+1} - \psi_{\alpha\beta-1}), \quad \text{and} \\ \gamma_{2C\alpha\beta} &= \frac{1}{4}(\psi_{\alpha+1\beta+1} + \psi_{\alpha-1\beta-1} - \psi_{\alpha+1\beta-1} - \psi_{\alpha-1\beta+1}). \end{aligned}$$

The index values  $\alpha, \beta = 1$  and  $\alpha, \beta = n$  correspond to opposite corners of a square field of view. The lensing parameters  $\kappa_{iC}$  and  $\gamma_{iC}$  at the positions of individual background galaxy images  $i$  are obtained by bilinear interpolation of their values on the adjacent grid points. They can therefore be expressed as linear combinations of the potential components:

$$\kappa_{iC} = \sum_{\gamma,\delta=0}^{n+1} a_{i\gamma\delta} \psi_{\gamma\delta} \quad \text{and} \quad \gamma_{iC} = \sum_{\gamma,\delta=0}^{n+1} b_{i\gamma\delta} \psi_{\gamma\delta}. \quad (1)$$

For each background galaxy image the coefficients  $a_{i\gamma\delta}$  and  $b_{i\gamma\delta}$  are non-zero only for 12, respectively 16, neighbouring grid points.

The total surface mass density  $\kappa_i$  and shear  $\gamma_i$  are calculated by adding the contributions  $\kappa_{iG_j}$  and  $\gamma_{iG_j}$  from the cluster galaxies  $G_j$  to those of the global cluster component:

$$\kappa_i = \kappa_{iC} + \sum_{j=1}^N \kappa_{iG_j} \quad \text{and} \quad \gamma_i = \gamma_{iC} + \sum_{j=1}^N \gamma_{iG_j}. \quad (2)$$

The values  $\kappa_{iG_j}$  and  $\gamma_{iG_j}$  depend on the relative positions of background images and cluster galaxies and, of course, on the mass distribution of the cluster galaxies. As in Paper I we use a truncated singular isothermal sphere as a model for their dark matter distribution and apply the scaling laws

$$\sigma = \sigma_* \left( \frac{L}{L_*} \right)^{1/\eta} \quad \text{and} \quad s = s_* \left( \frac{L}{L_*} \right)^\nu \quad (3)$$

with  $\eta = 4$  and  $\nu = 0.5$  to relate the model parameters to those of an  $L_*$ -galaxy with velocity dispersion  $\sigma_*$  and cut-off radius  $s_*$ . This choice of parametrization was critically discussed in Paper I and in practice different strategies could be more appropriate. However, the principles of the method described here do not depend on the details of the galaxy parametrization scheme, and for the rest of this section  $\sigma_*$  and  $s_*$  can be more generally interpreted as representing a given set of parameters used to describe the mass distribution of the cluster galaxies.

The likelihood function is defined as the product of the probability densities for the observed image ellipticities of the background galaxies:

$$\mathcal{L}(\sigma_*, s_*, \{\psi_{\alpha\beta}\}) = \prod_i p_\epsilon(\epsilon_i | \kappa_i, \gamma_i). \quad (4)$$

It depends on the galaxy parameters  $\sigma_*$  and  $s_*$  and on the description of the global cluster component provided by the potential values  $\psi_{\alpha\beta}$  on the grid points.

### 2.2 Probability density distributions

In Paper I we calculated and illustrated the probability density distribution  $p_\epsilon(\epsilon | \kappa_\infty, \gamma_\infty)$  for the image ellipticities of gravitationally lensed background galaxies. For the present method it turned out to be necessary to approximate  $p_\epsilon$  by a simple analytical function for numerical reasons.

In the case of a single redshift plane for the background galaxies, or if an estimate for the redshift of individual galaxies is available (e.g., photometric redshifts), the expectation value for image ellipticities is determined by the reduced shear:

$$\langle \epsilon \rangle_{\epsilon_s} = \hat{g} := \begin{cases} g & \text{for } |g| \leq 1 \\ 1/g^* & \text{for } |g| > 1. \end{cases} \quad (5)$$

Contours of the probability density distribution in the ellipticity parameter space  $\epsilon$  are fairly circular (see Fig. 5 of Paper I) and we show in Appendix A that the dispersion of the distribution in ‘shear direction’ is equal to the dispersion perpendicular to this direction in the ellipticity coordinates. Therefore, the Gaussian distribution

$$p_\epsilon(\epsilon | g) \approx \frac{1}{\pi \sigma_\epsilon^2(\hat{g})} e^{-\frac{|\epsilon - \hat{g}|^2}{\sigma_\epsilon^2(\hat{g})}} \quad (6)$$

represents a convenient approximation to the probability density distribution which reproduces its first and second moments. The dispersion  $\sigma_\epsilon(\tilde{g})$  as a function of  $\tilde{g}$  can be approximated by a simple analytical fit to numerical results similar to the discussion further below.

In the case of a redshift distribution for the source galaxies it is more difficult to specify simple expressions to approximate the probability density distributions. In this paper we restrict the application of our method to images located in non-critical regions of clusters. In this case we can use the approximation (Seitz & Schneider 1997)

$$\langle \epsilon \rangle_{\epsilon_{s,z}} \approx \frac{\langle w \rangle_z \gamma_\infty}{1 - \frac{\langle w^2 \rangle_z}{\langle w \rangle_z} \kappa_\infty}$$

for the expectation value of the image ellipticities. In the presence of a source redshift distribution the probability distribution for the image ellipticities is elongated in the ‘shear direction’ (see Fig. 5 of Paper I), i.e., the dispersion in this direction is larger than in the perpendicular direction. Hence we model the probability distribution with a Gaussian of the form

$$p_\epsilon(\epsilon | \kappa_\infty, \gamma_\infty) \approx \frac{1}{2\pi \sigma_{\tilde{\epsilon}_1}(\tilde{g}_r) \sigma_{\tilde{\epsilon}_2}(\tilde{g}_r)} \cdot e^{-\frac{1}{2} \frac{(\tilde{\epsilon}_1 - \tilde{g}_r)^2}{\sigma_{\tilde{\epsilon}_1}^2(\tilde{g}_r)} - \frac{1}{2} \frac{\tilde{\epsilon}_2^2}{\sigma_{\tilde{\epsilon}_2}^2(\tilde{g}_r)}}, \quad (7)$$

where  $\tilde{g}_r$  is defined as

$$\tilde{g}_r := \frac{\langle w \rangle_z |\gamma_\infty|}{1 - \frac{\langle w^2 \rangle_z}{\langle w \rangle_z} \kappa_\infty}, \quad \text{and} \quad \tilde{\epsilon} = \tilde{\epsilon}_1 + i\tilde{\epsilon}_2 := \frac{\gamma_\infty^*}{|\gamma_\infty|} \epsilon$$

expresses the image ellipticities in ‘local shear coordinates’, i.e., in a coordinate system in which the imaginary part of the (reduced) shear vanishes. We approximate the dependence of the dispersions  $\sigma_{\tilde{\epsilon}_1}$  and  $\sigma_{\tilde{\epsilon}_2}$  on  $\tilde{g}_r$  by quadratic functions:

$$\sigma_{\tilde{\epsilon}_1}(\tilde{g}_r) \approx \frac{1}{\sqrt{2}} \sigma_{\epsilon_s} + c_{11} \tilde{g}_r + c_{12} \tilde{g}_r^2, \quad \text{and} \\ \sigma_{\tilde{\epsilon}_2}(\tilde{g}_r) \approx \frac{1}{\sqrt{2}} \sigma_{\epsilon_s} + c_{21} \tilde{g}_r + c_{22} \tilde{g}_r^2.$$

For a given intrinsic ellipticity and redshift distribution of the sources the constants are determined by a fit to numerical results as shown in Fig. 1.

### 2.3 Likelihood maximization

The logarithm of the likelihood function is given by

$$l(\sigma_*, s_*, \{\psi_{\alpha\beta}\}) := \ln \mathcal{L} = \sum_i \ln p_\epsilon(\epsilon_i | \kappa_i, \gamma_i). \quad (8)$$

For a given set of cluster galaxy parameters  $(\sigma_*, s_*)$  the likelihood is maximized with respect to the potential values  $\psi_{\alpha\beta}$  on the grid points in order to determine the best representation of the global cluster component that is consistent with the presence of the cluster galaxies as specified by the model. Repeating this maximization procedure for varying galaxy parameters allows to determine the likelihood  $l(\sigma_*, s_*)$  as a function of the galaxy model and to derive confidence regions in the parameter space.

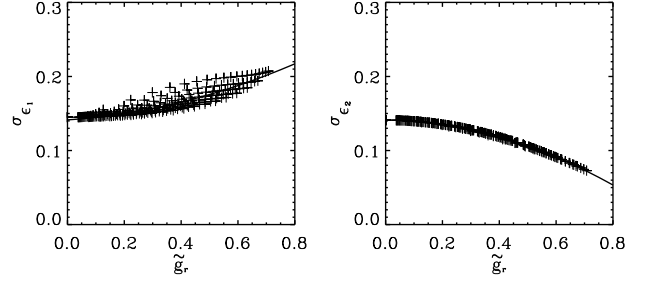


**Figure 1.** Approximations for the dispersion of the probability density  $p_\epsilon(\epsilon)$ . The dispersions  $\sigma_{\tilde{\epsilon}_1}$  and  $\sigma_{\tilde{\epsilon}_2}$  were calculated for a grid of parameter values of the quantities  $\kappa_\infty$  and  $|\gamma_\infty|$ . The crosses in the plots show the results as a function of  $\tilde{g}_r$  for all data points with  $|g_\infty| < 1$ . The solid lines show fits to these data points using quadratic functions. The results displayed in this figure were calculated for the intrinsic ellipticity ( $\sigma_{\epsilon_s} = 0.2$ ) and redshift distributions that were used in the simulations of Paper I.

Specifying the parameters for the galaxy mass model determines the mass  $M_G$  contained in galaxies in absolute numbers:

$$M_G(\sigma_*, s_*) = \sum_{j=1}^N M_{Gj}(L_j, \sigma_*, s_*). \quad (9)$$

Here  $L_j$  denotes the cluster galaxy luminosity, but it can be more generally interpreted as representing a set of galaxy characteristics that are used to specify the mass model for individual galaxies. On the other hand, the total mass  $M$  of the galaxy cluster, or equivalently the average surface mass density  $\bar{\kappa}_\infty$ , is provided by a mass reconstruction. The likelihood function defined above only uses information on the shapes of background images and therefore it is invariant under the mass sheet transformation (see Paper I). However, we assume that this degeneracy can be broken by other means and so the total cluster mass within the field of view is fixed. In order to include the information on the total mass into the maximization procedure we adopt the following strategy: The fraction of mass contained in the global cluster component and not associated with galaxies is denoted as  $f_C(\sigma_*, s_*) := 1 - M_G(\sigma_*, s_*)/M$  and depends on the galaxy model parameters. Multiplication of the likelihood function with the factor

$$p_{\bar{\kappa}_C}(\bar{\kappa}_C) = \frac{1}{\sigma_{\bar{\kappa}_C} \sqrt{2\pi}} e^{-\frac{1}{2} \frac{(\bar{\kappa}_C - f_C \bar{\kappa}_\infty)^2}{\sigma_{\bar{\kappa}_C}^2}} \quad (10)$$

ensures that the average surface mass density

$$\bar{\kappa}_C = \frac{1}{n^2} \sum_{\alpha, \beta=1}^n \kappa_{C\alpha\beta}$$

of the reconstructed global cluster component reproduces the correct mass fraction  $f_C(\sigma_*, s_*)$ . This corresponds to adding the term

$$l_{\bar{\kappa}_C} = \ln p_{\bar{\kappa}_C} = -\frac{(\bar{\kappa}_C - f_C \bar{\kappa}_\infty)^2}{2\sigma_{\bar{\kappa}_C}^2} + \text{constant} \quad (11)$$

to the logarithm of the likelihood. The value of the parameter  $\sigma_{\bar{\kappa}_C}$  is only of numerical interest and has been chosen as 0.001 for the applications described later in this paper.

The lensing quantities, surface mass density and shear, are second derivatives of the potential  $\psi_\infty$ , and therefore adding linear functions to the potential does not change the mass distribution and the likelihood. It turned out that the presence of these invariance transformations does not cause practical problems in our implementation of the method. In principle they can be suppressed during the maximization procedure, for example by fixing the potential values at three corners of the field of view as in Bartelmann et al. (1996).

In order to prevent the cluster component from fitting noise and from exhibiting structures on small scales we also add an entropy-like regularization term of the form

$$S = \sum_{\alpha,\beta=1}^n \ln \hat{\kappa}_{C\alpha\beta} \quad (12)$$

(see e.g. Narayan & Nityananda 1986) with

$$\hat{\kappa}_{C\alpha\beta} = \tilde{\kappa}_{C\alpha\beta} / \sum_{\gamma,\delta=1}^n \tilde{\kappa}_{C\gamma\delta} \quad \text{and} \quad \tilde{\kappa}_{C\alpha\beta} = \kappa_{C\alpha\beta} / \kappa_{P\alpha\beta}$$

to the logarithm of the likelihood function. An additional benefit of this regularization term is that it ensures the reconstructed surface mass density to be positive. The factor  $\kappa_{P\alpha\beta}$  allows to include prior information on the mass distribution into the regularization.

A conjugate gradient algorithm from Press et al. (1992) is then used in order to maximize the quantity

$$\hat{l}(\sigma_*, s_*, \{\psi_{\alpha\beta}\}) := l + l_{\tilde{\kappa}_C} + \lambda S. \quad (13)$$

This algorithm makes use of the derivatives  $\partial \hat{l} / \partial \psi_{\alpha\beta}$  which are straightforward to compute analytically (see Appendix B). The choice of the regularization parameter  $\lambda$  allows to adjust the result between a pure likelihood maximization and a reproduction of the prior mass distribution. In general we use the mass distribution from a conventional reconstruction as the prior. In addition, we calculate the potential  $\psi_{P\alpha\beta}$  corresponding to this conventional reconstruction and use  $f_C(\sigma_*, s_*) \psi_{P\alpha\beta}$  as the start value for the maximization algorithm. This guarantees the correct mass fraction for the start value of the cluster component as a function of the galaxy model parameters and therefore reduces the computational effort for the maximization procedure.

### 3 APPLICATION TO SIMULATIONS

In Paper I we divided the data of our simulations into two subsets according to the position of the background galaxies within the field of view: A central sub-field containing the highly non-linear lensing regime, and the outskirts of the cluster where the surface mass density is comparatively low. For computational reasons we restrict the application of the generalized likelihood method presented in this paper to the central data region that covers  $2'5 \times 2'5$  and includes roughly 90 cluster galaxies and 240 background galaxies. We use a conventional inversion method as explained in Paper I to reconstruct the mass distribution within the total field of view ( $10' \times 10'$ ) of the simulations. The lensing potential  $\psi_\infty$  can be determined by integrating the surface mass density appropriately. We then apply the likelihood procedure described in the previous section taking the surface mass

density and the potential in the central sub-field as regularization prior and start value, respectively. The reconstructed mass distribution also specifies the average  $\bar{\kappa}_\infty = 0.32$  of the total surface mass density within the sub-field, which is required for the term  $l_{\tilde{\kappa}_C}$  ensuring the correct total mass.

We explore the dependence of  $l$  on the galaxy parameters, velocity dispersion  $\sigma_*$  and cut-off radius  $s_*$ , by maximizing the quantity  $\hat{l}(\sigma_*, s_*)$  with respect to the potential values on the grid points. Fig. 2 shows confidence regions resulting from these calculations for the same realizations of cluster and background galaxies as in Paper I. The number of grid points used here is  $5 \times 5$  which corresponds to a grid point separation of  $68h^{-1}$  kpc. This provides sufficient resolution for an adequate description of the global cluster mass distribution that had been used as an input for the simulations. The value of the regularization parameter was chosen as  $\lambda = 1$ .

A comparison of the results for the input model with small galaxy haloes ( $s_* = 3.4h^{-1}$  kpc) to those of Paper I shows that the confidence regions for the galaxy parameters within the plotted range are very similar, but more extended with the new method. The simpler approach of Paper I provides satisfying results when testing model parameters that imply a small fraction of the total mass in galaxies. For increasing galaxy mass fraction, however, the difference between the (appropriately scaled) conventional mass reconstruction and the concept of a global underlying cluster mass component becomes larger. In the new method the cluster component can adapt to the presence of potentially massive galaxies and redistribute the matter in the cluster component accordingly. The additional degrees of freedom lead to the larger extension of the confidence regions for increasing  $s_*$ -values. (As in Paper I the range of the cut-off radius parameter was confined to small values in the plots in order to emphasize the structure of the confidence regions close to the input value, and because the inclusion of prior information on the velocity dispersion as discussed in Paper I could rule out large values for the cut-off radius in this case.)

In the model with  $s_* = 34h^{-1}$  kpc the galaxies contain a considerable fraction of the total mass of the system. In Paper I we investigated strategies for subtracting the galaxy masses from a conventional cluster reconstruction in order to use it as a description of the ‘global cluster component’ in the likelihood method described there. For the highly non-linear lensing regime in the cluster centre, however, this proved to be very difficult and the resulting confidence regions for the galaxy parameters turned out to be rather sensitive to the details of the subtraction procedure. These problems are nicely resolved by applying the generalized likelihood method presented in this paper, which takes the presence of the galaxies explicitly into account when determining the best representation of the global cluster component for a given galaxy model. As discussed in Paper I the quantity that can be determined best with this lensing method is the mass within the projected radius that corresponds to about the closest separation between cluster and background galaxies used in the analysis. As expected the confidence regions resulting with the new method are extended along lines of equal mass within this radius. Due to the freedom of the cluster component to adapt to the galaxy model, the extension of the confidence regions is larger than in the respective plots of Paper I.

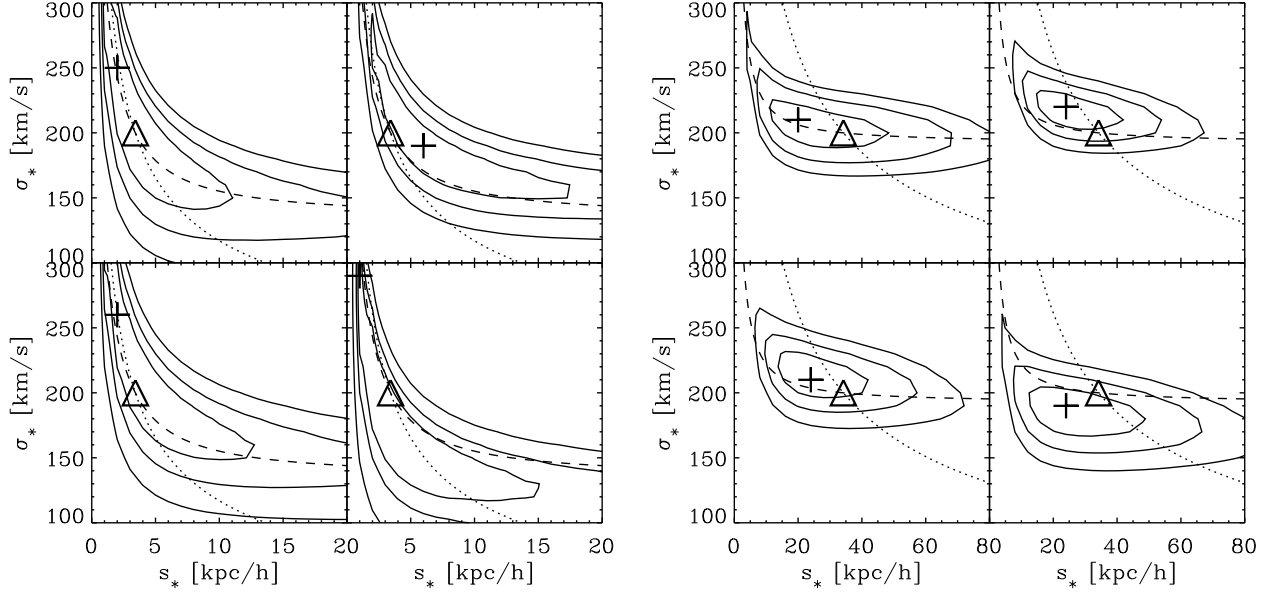


**Figure 2.** Confidence regions for the velocity dispersion and the cut-off radius calculated with the method described in this paper using a  $5 \times 5$  grid and the regularization parameter  $\lambda = 1$ . The four different realizations of simulated observational data are the same as in Paper I. This figure should be compared with the bottom sets of plots in Fig. 7 of Paper I. The plots on the **left** are for the galaxy input model with a cut-off radius of  $s_* = 3.4h^{-1}$  kpc, and the plots on the **right** are for  $s_* = 34h^{-1}$  kpc. The confidence contours are 99.73%, 95.4%, and 68.3%, determined in the way explained in Paper I (without prior information). The triangle denotes the input values and the cross marks the maximum of the likelihood function. The dotted line connects models with equal total mass, and along the dashed line the mass within a projected radius of  $5.4h^{-1}$  kpc is constant.

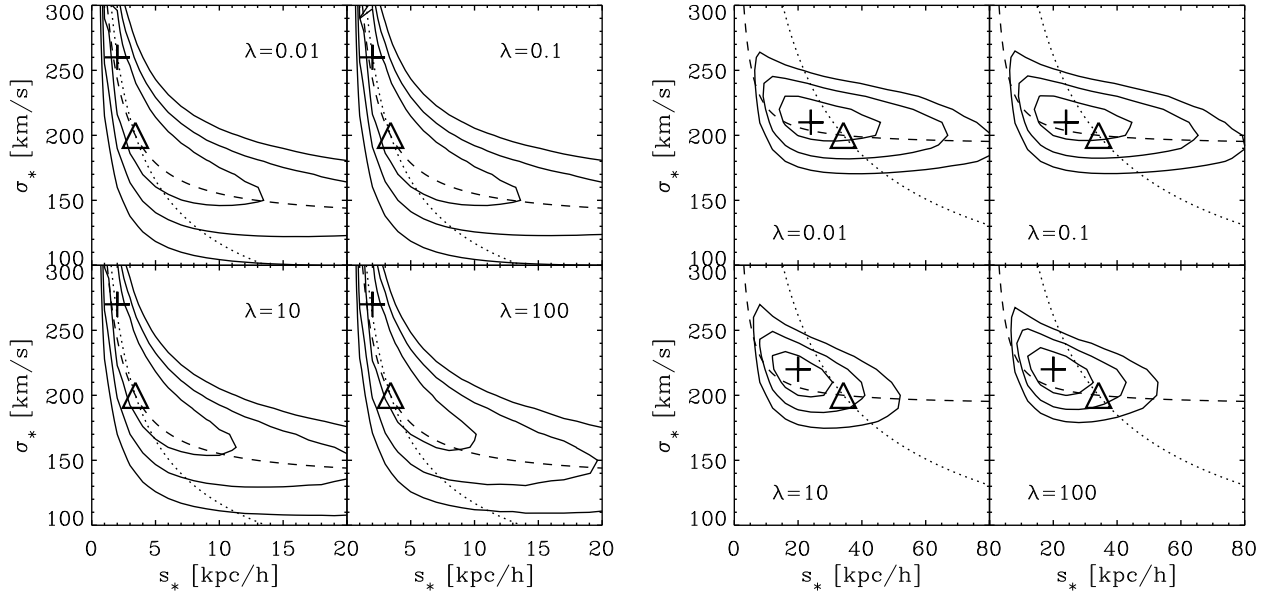


**Figure 3.** Dependence of the confidence contours on the regularization parameter  $\lambda$ . The random realization of cluster and background galaxies is the same as for the bottom left plots in the panels of Fig. 2. The values for  $\lambda$  are 0.01 (**top left**), 0.1 (**top right**), 10 (**bottom left**) and 100 (**bottom right**). The number of grid points is  $5 \times 5$ . The significance of the contours and the meaning of the symbols is analogous to Fig. 2.

In Fig. 3 we investigated the sensitivity of the results to the choice of the regularization parameter. For large values of  $\lambda$  the ‘prejudice’ that is provided by the conventional reconstruction and that enters the method as the regularization prior, is highly weighted and dominates over the likelihood term in equation (13). Regularizing too strongly there-

fore leads to the same kind of problems as discussed for the method of Paper I, and the confidence regions approach the solution of Paper I for  $\lambda \rightarrow \infty$ . This trend is more obvious for the input model with massive galaxies ( $s_* = 34h^{-1}$  kpc), where the difference between the results of the two methods is larger. Reducing  $\lambda$  enables the cluster component to adapt

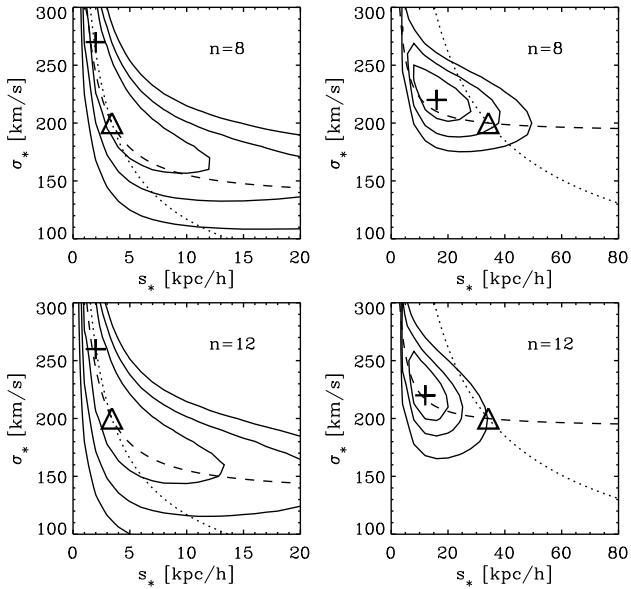


**Figure 4.** Dependence of the confidence contours on the number of grid points. The random realization of cluster and background galaxies is the same as for the bottom left plots of Fig. 2. The **top** plots are for an  $8 \times 8$  grid, and in the **bottom** plots a  $12 \times 12$  grid was used. The regularization parameter is  $\lambda = 1$ . The significance of the contours and the meaning of the symbols is analogous to the previous figures.

to changes in the prescription for the galaxy model more liberally by maximizing the likelihood term  $l$ , and hence leads to a larger extension of the confidence regions for the galaxy parameters. We discuss the question for the optimal choice of the regularization parameter below in context with the evolution of the absolute likelihood value.

Fig. 4 displays confidence contours calculated with a finer grid for describing the lensing potential of the cluster component. An  $8 \times 8$  grid corresponds to a grid point separation of  $39h^{-1}$  kpc, and a  $12 \times 12$  grid gives  $25h^{-1}$  kpc. In the case of the galaxy model with small cut-off radius the result shown here is only slightly affected by changing the grid, because the parameter range for the cut-off radius covered by the plots still remains smaller than the grid point separation. In the model with extended ( $s_* = 34h^{-1}$  kpc) dark matter haloes for the cluster galaxies, however, a refined grid resolution already enables the cluster component to adapt within a certain extent to the large haloes of luminous cluster galaxies. Models with a larger fraction of the mass in the cluster component and smaller galaxy mass fraction have more freedom to adjust to noise. This leads to a shift of the maximum likelihood solution towards lower values for the  $s_*$ -parameter and biases against high cut-off radius values for which a large mass fraction is fixed in galaxies and not available to fit noise. Solving this problem by applying a stronger regularization to prevent the cluster component from fitting structures on ‘galaxy scales’ is not straightforward because this increases the weight given to the conventional reconstruction and leads to the same problems as mentioned above. In order to reliably retrieve the input values of the simulations even with small grid point separations, it could be useful to explore strategies in which the prior is adapted during the maximization process. How-

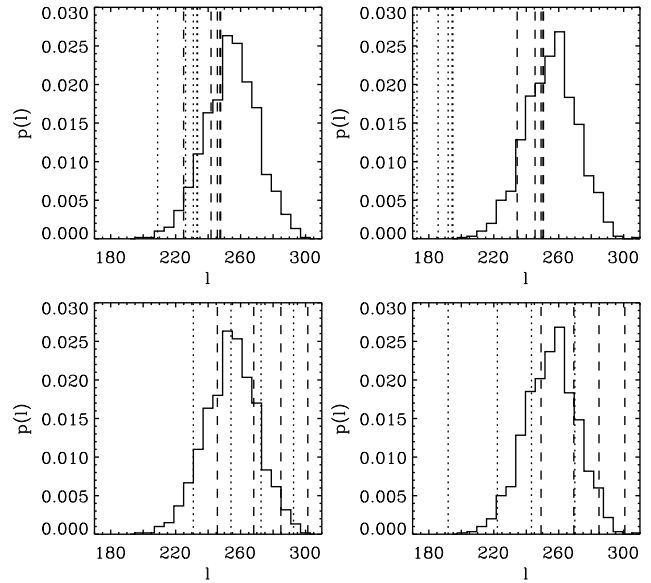


**Figure 5.** Dependence of the maximum likelihood value on the regularization parameter and on the number of grid points. The histograms show the probability distribution of the maximum  $\text{Max}(l)$  of the logarithm of the likelihood function calculated from the correct input mass distribution and many different galaxy realizations. The plots on the **left** are for the galaxy input model with a cut-off radius of  $s_* = 3.4h^{-1}$  kpc, and the plots on the **right** are for  $s_* = 34h^{-1}$  kpc. Dashed vertical lines indicate the value of  $l$  at the maximum of the likelihood function, and dotted vertical lines denote its value for a reconstruction without cluster galaxies. The **bottom** plots depict the dependence on the number of grid points for  $\lambda = 1$ . With increasing  $l$  the lines represent a  $5 \times 5$ ,  $8 \times 8$ ,  $10 \times 10$ , and  $12 \times 12$  grid. The **top** diagrams show the dependence on the regularization parameter for a  $5 \times 5$  grid. With increasing  $l$  the lines are for  $\lambda = 100$ ,  $10$ ,  $1$ ,  $0.1$ , and  $0.01$ . However, the latter likelihood values are close together, and so the last two or three lines cannot be distinguished in this representation. [The values for  $\text{Max}(l)$  indicated by the vertical lines were calculated using equation (7) for the probability distribution of image ellipticities, whereas the histograms were determined without this approximation. The differences between approximation and exact calculation are small and do not change any of the conclusions drawn in the text.]

ever, it is a much more pragmatic point of view to accept these difficulties as a manifestation of the fundamental conceptual problem of making a clear-cut distinction between the galaxy mass distribution and a global cluster component. In this philosophy the grid point distance provides the scale for a technical separation of the galaxies from a more general mass component.

Finally Fig. 5 depicts the evolution of the maximum  $\text{Max}(l)$  of the logarithm of the likelihood function when changing the regularization parameter and the number of grid points. In the case of the  $5 \times 5$  grid the rather large separation between the grid points already provides some kind of regularization to prevent the cluster component from fitting noise. Decreasing  $\lambda$  increases the maximum of the likelihood function only slightly, and  $\text{Max}(l)$  stays within the probability distribution  $p(l)$  for the logarithm of the likelihood that indicates statistical consistency with a correct description of the mass distribution. Although the mass reconstructions

within the range of regularization values tested here ( $\lambda = 0.01 - 100$ ) are all statistically consistent with the observables in an absolute likelihood sense, we consider  $\lambda = 1$  as the optimal value providing the most reliable results for the analysis of our simulations. Regularizing too strongly causes the problems that were discussed above. Very small  $\lambda$  values lead to an extension of the likelihood contours in the direction of very high values for the cut-off radius parameter (see Fig. 3). Visual inspection of the reconstructed cluster component for these large cut-off radius solutions reveals strongly fluctuating mass distributions which obviously fit noise.

Increasing the number of grid points allows the cluster component to adjust to smaller structures, but it also increases the tendency to fit noise. The dependence of  $\text{Max}(l)$  on the grid size (for fixed  $\lambda$ ) is much stronger than its dependence on the regularization parameter. For a  $12 \times 12$  grid with  $\lambda = 1$  the value of  $\text{Max}(l)$  is already far in the tail of its expected distribution, which suggests that small scale structures in the mass distribution of the reconstructed cluster component mainly consist of noise. To compensate this effect one would need to increase the regularization strength. The figure also shows that in the case of extended dark matter haloes for the galaxies, the difference in the likelihood values between the best reconstruction with galaxies and a reconstruction without galaxies is much larger than for the input model with small cut-off radius for the cluster galaxies.

## 4 APPLICATION TO CL0939+4713

### 4.1 Cluster reconstruction

We test the method described above on a WFPC2 image (Dressler et al. 1994b) of the cluster Cl0939+4713. From these observations Seitz et al. (1996, hereafter SKSS) obtained a reconstruction of the cluster mass distribution by applying a non-linear finite-field inversion algorithm. We use their galaxy catalogue which supplies positions, ellipticities, and  $R$  magnitudes. The cluster is at a relatively high redshift of  $z_d = 0.41$ . This means that the normalization of the reconstructed mass distribution is rather sensitive to the unknown redshift distribution of the faint galaxies that are used as sources. In addition, due to the small field of view which contains the central cluster region only, it is not possible to break the mass sheet transformation by assuming negligible surface mass density values at the boundaries. The lack of colour information for the objects detected in the field also makes it difficult to break this degeneracy by using magnification effects on the number counts or on the sizes of the background galaxies. SKSS investigated the implications of these problems on their cluster reconstruction. Here we restrict the calculations to assumptions for the relevant parameters and qualitatively discuss the effects of changing them afterwards. The cluster is marginally critical and contains an arc as well as a multiple image system of a source galaxy located at a redshift of 3.98 (Trager et al. 1997). The extension of the critical region is very small compared to the total area of the field, and so we exclude it from our analysis.

We consider all galaxies in the magnitude interval  $R \in [23.5, 25.5]$  that fulfill the observational selection criteria of SKSS as sources. However, we exclude three objects whose

images are located between the central cluster galaxies and are therefore likely to lie in the critical region. In total we use 276 galaxy images. Fig. 6 shows the spatial distribution of this population and the ellipticity field that was calculated from their shapes by employing an averaging procedure with a scale of  $20''$ . We assume a source redshift distribution of the same form as it was used for our simulations, i.e., equation (10) of Paper I with the parameters  $\langle z \rangle = 1$  and  $\beta = 1$ . This gives a value of  $\langle w \rangle = 0.44$  for the average relative lensing strength (we use  $\Omega = 1$  and  $\Lambda = 0$ ). In analogy to SKSS we reconstruct the cluster mass from the ellipticity field by applying the methods developed in Seitz & Schneider (1996) and Seitz & Schneider (1997). Our result is consistent with theirs. We scale the reconstructed mass distribution such that the average surface mass density is  $\bar{\kappa}_\infty = 0.35$  by using the mass sheet transformation in the form generalized to a redshift distribution of the sources (Seitz & Schneider 1997). This gives a total mass of  $1.97 \times 10^{14} h^{-1} M_\odot$  within the field of view.

We calculate the lensing potential from the surface mass density. This involves an integration that formally extends over the whole lens plane, whereas the data region is limited. The shear contribution provided by the matter outside of the field of view cannot be neglected here, because the surface mass density values are still appreciable at the boundary. We extrapolate the reconstructed mass distribution with a simple linear prescription outside of the data region before calculating the potential  $\psi_{\alpha\beta}$  on a grid. Therefore, the result correctly describes the mass distribution in the field of view as it was determined from the reconstruction, but it contains only an approximate description of the shear. Nevertheless, it serves as a reasonable start value for the maximum likelihood algorithm. The arbitrary element introduced by the extrapolation procedure is then of course resolved during the likelihood maximization which adjusts the potential such that the shear is optimally reproduced. We use the surface mass density values on the grid points calculated from the initial potential grid as the regularization prior  $\kappa_{P\alpha\beta}$ . The missing quadrant of the wide field camera does not cause a problem for the technical implementation of the method. The potential values on the irrelevant grid points are excluded from the maximization procedure. The calculation of the entropy  $S$  and the average surface mass density  $\bar{\kappa}_C$  is restricted to the data region. For the probability distribution of image ellipticities the approximation (7) is applied with dispersions calculated in analogy to Fig. 1, taking into account the different cluster redshift and using the same intrinsic ellipticity dispersion of  $\sigma_{\epsilon_s} = 0.2$  as for the simulations.

Fig. 6 shows maximum likelihood reconstructions of the cluster Cl0939+4713 that were performed with our algorithm without taking the presence of the cluster galaxies into account. Using a  $6 \times 6$  grid for the surface mass density gives a grid point separation of  $101 h^{-1} \text{ kpc}$  and allows to resolve the main features characterizing the mass distribution. As discussed by SKSS the two mass maxima in the bottom quadrants and the minimum in the top right quadrant tend to correlate with the distribution of bright galaxies. This trend is also visible in the diagram depicting the distribution of our cluster galaxy sample which will be defined below. The galaxies in the top right quadrant are mainly less bright spirals and a substantial fraction of

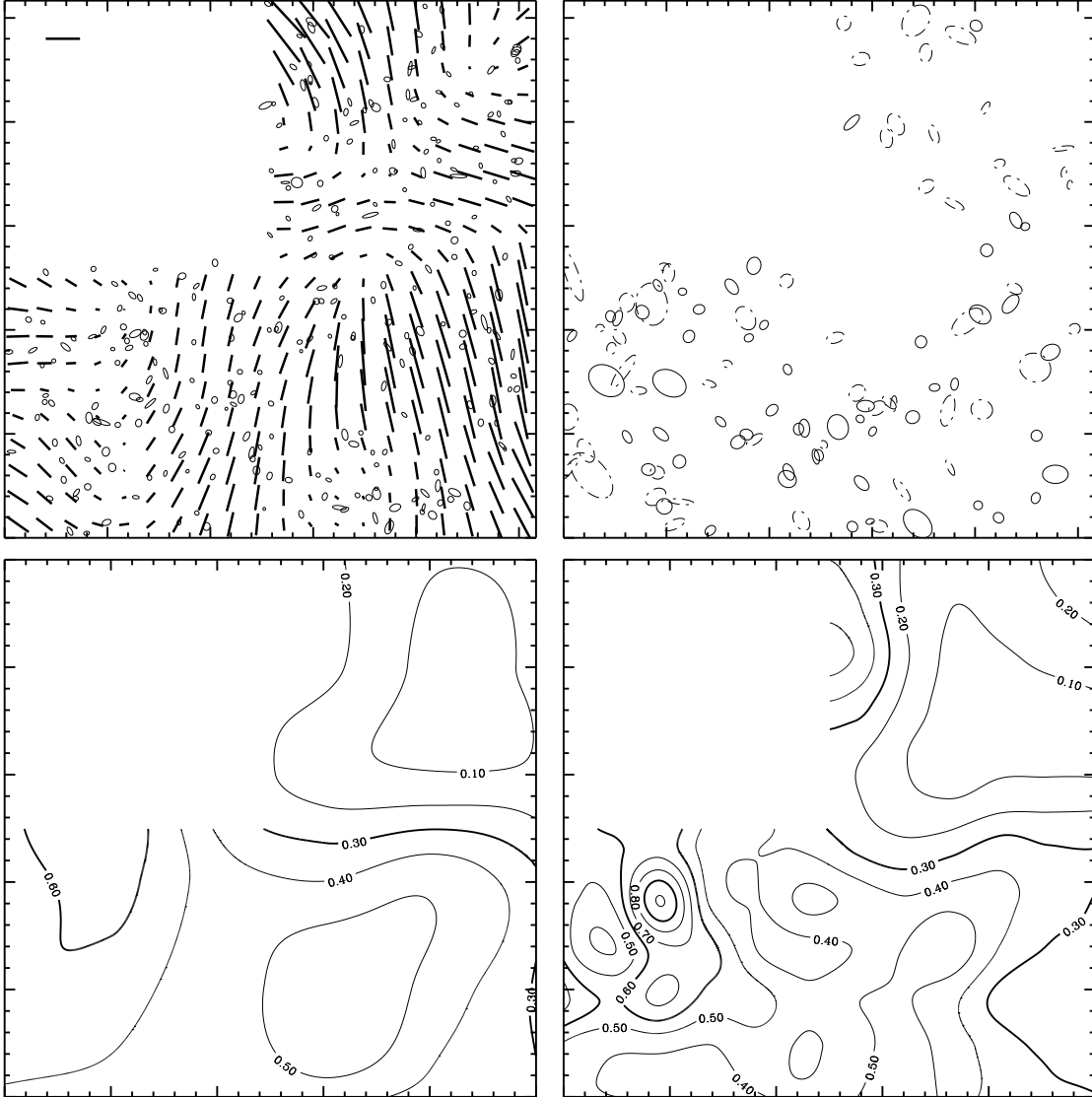


**Figure 6.** The galaxy and mass distribution in the WFPC2 field of the cluster Cl0939+4713. The **top left** plot displays the galaxies in the magnitude interval  $R \in [23.5, 25.5]$  which were used as sources for the weak lensing analysis. Each galaxy is represented by an ellipse which indicates its ellipticity, position angle and relative size. Superposed on these individual galaxy images is their average ellipticity field on a  $20 \times 20$  grid. The length of the bar in the top left corner of this plot corresponds to an average ellipticity of  $|\bar{e}| = 0.1$ . The **top right** plot shows all the galaxies that were included as cluster galaxies in our analysis. The ellipses drawn with solid lines represent objects which were classified as E- or S0-galaxies in Smail et al. (1997), and the broken lines indicate those classified as spiral or irregular galaxies. The **bottom** plots depict reconstructions of the cluster mass distribution using our maximum likelihood method without including the presence of cluster galaxies. The **left** plot was produced with a  $6 \times 6$  grid, and the plot on the **right** was obtained with a  $12 \times 12$  grid. For the purpose of this representation the reconstructions have been bicubically interpolated on a finer grid before using the contour plot program. The regularization parameter was  $\lambda = 10$ . The contour lines depict the surface mass density values  $\kappa_\infty = 0.1, 0.2, 0.3, \dots, 1.0$ . The mass sheet degeneracy was artificially adjusted such that the average surface mass density in the data region is  $\bar{\kappa}_\infty = 0.35$ . The side length of the field of view is  $2'.58$  which corresponds to  $505h^{-1}$  kpc at the cluster redshift of  $z_d = 0.41$ . (We assume  $\Omega = 1$  and  $\Lambda = 0$  in this paper.)

them might not be cluster members. A  $12 \times 12$  grid with a grid point separation of  $46h^{-1}$  kpc enables the mass distribution to adjust to smaller structures. The weak lensing reconstruction now produces a high mass peak roughly at the position of the strong lensing features. The height of this maximum depends on the regularization strength. Its exact position depends on the number of grid points, because in the method maxima can obviously only occur at

grid points. The positional uncertainty of the mass peak is such that its location is consistent with coinciding with the strong lensing region. SKSS were not able to provide evidence for such a rather steep increase of the surface mass density at this position, because inversion algorithms which rely on the averaged ellipticity field as input tend to smear out such features, whereas the maximum likelihood method applied here uses the individual image ellipticities directly



as observables (see also Seitz et al. 1998). However, the reliability of the smaller scale structures in this mass map is doubtful and their significance is difficult to estimate. We will come back to this question at the end of the next section in context with a discussion of the absolute likelihood value.

The strong lensing features are caused by the joint effects of a global cluster component and several bright cluster galaxies located in the cluster centre. We do not attempt to reproduce the multiple image system here, because the spatial resolution reliably accessible to the non-parametric reconstruction is considerably larger than the image separation. This also means that it is very difficult to use the strong lensing information for breaking the mass sheet degeneracy and to determine the slope of the central cluster profile in this case.

## 4.2 Cluster galaxy analysis

To select cluster galaxies we used the morphological classification and instrumental magnitudes ( $R_{702}$ ) provided by Smail et al. (1997). Galaxies that were denoted as ‘compact’ or ‘unclassifiable’, or for which measured redshifts from Dressler & Gunn (1992) exclude a cluster membership, were not taken into account. We define an  $L_*$ -galaxy by requiring an absolute V-magnitude of  $-20.5 + 5 \log h$  (corresponding to  $m_V = 20.2$ ), which is close to the value determined by Smail et al. (1997) from a fit to the luminosity function of elliptical galaxies in clusters of this redshift range. For direct comparison we take the same value for spiral galaxies as well. For the cluster redshift of  $z_d = 0.41$  the R-band filter probes roughly the same spectral range as a rest frame V-band filter, and the correction factors for the conversion of these filters are small (B. Ziegler, private communication). For our cluster galaxy sample we therefore identify R-magnitudes from the catalogue with rest-frame V-magnitudes. Possible systematic errors introduced by this simplification are in any case smaller than those resulting from other problems that will be discussed later. As in our simulations we only include galaxies with a luminosity brighter than  $0.1L_*$  ( $m_V < 22.7$ ) in our analysis, because very faint cluster galaxies do not contribute much to the lensing signal. According to the morphological classification we divide our sample into two subsets. One of them includes 56 elliptical and S0-galaxies and the other contains 55 objects classified as spiral or irregular galaxies. Fig. 6 schematically displays the galaxies that were included in our cluster galaxy sample. It is very likely that some of the objects in the sample are in fact foreground galaxies and the implications of this problem on the results of the lensing analysis will be discussed below. Fig. 4 of Dressler et al. (1994a) and Fig. 6 of Belloni et al. (1995) suggest that especially in the spiral galaxy subset a significant fraction could be interloping field galaxies.

Fig. 7 displays the results of applying the galaxy-galaxy lensing method developed in Section 2. Here we chose a  $6 \times 6$  grid for the cluster mass distribution which provides sufficient resolution for an adequate description of the reliably reconstructed features. As a start value for the potential  $\psi_{\alpha\beta}$  we took the maximum likelihood solution without galaxies that has been discussed in the previous section. In addition, the corresponding cluster mass distribution was taken as the regularization prior. The regularization parameter was

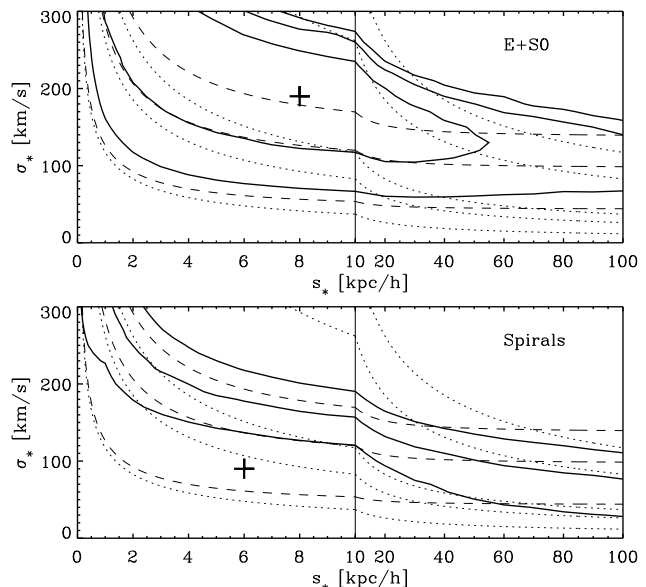


**Figure 7.** Results of applying the galaxy-galaxy lensing method presented in this paper to a WFC2 image of the cluster Cl0939+4713. The **top** plot shows confidence contours for the parameters describing the halo properties of an ensemble of 56 elliptical cluster galaxies, and the **bottom** plot is for 55 spiral galaxies. Note the change of scale at  $s_* = 10h^{-1}$  kpc. The calculations were performed with a  $6 \times 6$  grid for the cluster mass distribution, a regularization parameter of  $\lambda = 100$ , and the values  $\eta = 4$  and  $\nu = 0.5$  for the parameters of the scaling laws relating the properties of galaxies with different luminosities to those of an  $L_*$ -galaxies, which we defined as having an absolute V-magnitude of  $-20.5 + 5 \log h$ . The likelihood function includes shape information from 276 background galaxy images. The confidence contours are 99.73%, 95.4%, and 68.3%, determined in the way explained in Paper I, and the cross marks the maximum of the likelihood function. The dashed lines connect models with an equal aperture mass of  $M_*( < 8h^{-1} \text{ kpc} ) = 0.1, 0.5, \text{ and } 1.0 \times 10^{11} h^{-1} M_\odot$ , respectively. Similarly, the dotted lines are for a total  $L_*$ -galaxy mass of  $M_* = 0.1, 0.5, 1.0, 5.0 \text{ and } 10 \times 10^{11} h^{-1} M_\odot$ , which corresponds to a ‘galaxy mass fraction’ of 0.15%, 0.75%, 1.5%, 7.5% and 15%, respectively. *As discussed in the text, the results displayed here depend on assumptions regarding the redshift distribution of the sources and the mass sheet transformation! Changing these assumptions mainly leads to a shift of the confidence contours in  $\sigma_*$ -direction.*

chosen as  $\lambda = 100$ . In analogy to our simulations we use the scaling laws (3) to relate the velocity dispersion and the cut-off radius of galaxies with different luminosity to those of an  $L_*$ -galaxy, and we fix the scaling indices at the values  $\eta = 4$  and  $\nu = 0.5$ . We performed the calculation for the ensemble of 56 elliptical galaxies ignoring the presence of the spiral galaxies at first. For given values of the galaxy model parameters the method searches for the best representation of the remaining cluster mass component leaving the total mass of the system constant. Reassuringly, the resulting likelihood contours for the galaxy model parameters  $\sigma_*$  and  $s_*$  show qualitatively the same properties as in our simulations. Despite the small number of lens and source galaxies, the lensing effects of the elliptical cluster galaxies are detected with high significance: Reducing the mass of the cluster component and putting it into galaxies increases the

likelihood of the observed image ellipticities of background galaxies. As expected, the likelihood contours are extended along lines connecting models that imply equal mass for an  $L_*$ -galaxy within some characteristic radius. We empirically determined a value of  $8h^{-1}$  kpc by adjusting the dashed lines in the figure to the shape of the confidence contours in the low- $s_*$  region of the plot. Therefore the mass within this radius is the best-determined quantity from this analysis.

The figure also includes the result of an equivalent analysis of the spiral galaxy sample. In contrast to the ellipticals we do not find a signal in this case, although the number of galaxies and the range of luminosities are comparable for the two sets of galaxies. However, there is a factor of  $\sqrt{2}$  difference between the characteristic velocity dispersion parameter for elliptical and spiral galaxies of the same luminosity. This translates into a factor of two difference in the expected strength of the lensing effects, and so it is not surprising that the result is weaker for the spiral galaxy sample. As was mentioned above some of the spirals in this sample might actually be background galaxies, whereas we are interested in the properties of cluster galaxies here. Of course this could lead to a bias of the result, simply because they are the wrong kind of objects included in the sample, but also because their size and luminosity, as well as the strength of their lensing effects on the population of faint source galaxies would then be different than tested by the model, which assumes that they are located at the cluster redshift. In contrast to that, not taking into account cluster galaxies, which actually are present, does not introduce systematic effects: Repeating the above calculation of the confidence contours for spirals and ellipticals with inclusion of the best-fit model for the other galaxy type only leads to negligible changes of the result. The fact that non-cluster galaxies that were misclassified as cluster members can cause systematic effects whereas leaving out genuine cluster members does not, suggests that it is useful to apply conservative selection criteria for defining the cluster galaxy sample.

We checked the sensitivity of the result to changes of the regularization strength or the number of grid points that are used to describe the cluster potential. Fig. 8 displays the confidence contours for a reduced regularization parameter of  $\lambda = 10$  (keeping a  $6 \times 6$  grid), as well as for an  $8 \times 8$  grid for the cluster component (keeping  $\lambda = 100$ ). These calculations necessitate a larger amount of computation time than those performed for Fig. 7. The appearance of the confidence regions does not change very much with respect to our previous result. Now the axes of the plots are outside of the 99.73% confidence contour in both cases. (The axes correspond to model parameters implying zero mass in galaxies and therefore represent a pure cluster mass reconstruction without cluster galaxies.) This means that the galaxy-galaxy lensing signal becomes slightly more significant when the ability of the cluster component to adjust to the presence of the cluster galaxies is increased either by improving the resolution or by reducing the regularization strength. The confidence contours in Fig. 8 (but not those in Fig. 7) have been slightly smoothed in order to erase some discontinuities caused by a premature stopping of the maximization algorithm for some parameter values. This becomes a more serious problem for a larger number of grid points or a smaller regularization parameter. For the refined resolution achieved with the  $8 \times 8$  grid, which corresponds

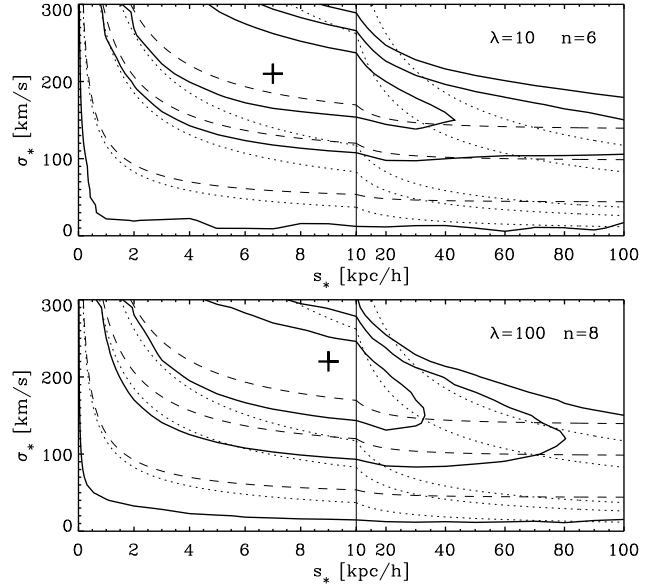


**Figure 8.** Dependence of the result for elliptical cluster galaxies on the number of grid points and the regularization strength. The **top** plot is for  $\lambda = 10$  with a  $6 \times 6$  grid, and the **bottom** one for  $\lambda = 100$  with an  $8 \times 8$  grid. The significance of the contours and the meaning of the lines is analogous to the previous figure.

to a grid point separation of  $72h^{-1}$  kpc, the confidence contours are less extended along the cut-off radius coordinate. As we discussed in Section 3 this effect can be explained by the ability of the cluster component to adapt to mass structures on scales comparable to the largest cut-off radius values shown in the plot.

To perform our analysis we were obliged to make assumptions on the redshift distribution of the faint objects in our background galaxy sample. Underestimating the source redshifts leads to an overestimate of the lens masses and therefore to a shift of the cluster galaxy confidence contours towards higher values for the velocity dispersion parameter. Conversely, overestimating the source redshifts leads to an underestimate of the galaxy masses. However, in our application the mass sheet degeneracy constitutes an additional complication. We broke this degeneracy artificially by fixing the average surface mass density at the value  $\bar{\kappa}_\infty = 0.35$ . For the redshift distribution that we have assumed this is roughly the minimal value that ensures that the mass density is non-negative over the whole field of view. Changing the assumptions for the redshift distribution leads to a change of the minimal possible value for the source redshift-independent quantity  $\bar{\kappa}_\infty$ . Equally viable solutions with larger  $\bar{\kappa}_\infty$  provide more convergence and require smaller variations in the mass distribution – and thus smaller galaxy masses – to produce the same observable image distortions. Adjusting  $\bar{\kappa}_\infty$  therefore allows to scale the resulting confidence contours for the cluster galaxy model parameters in the direction of the  $\sigma_*$ -axis of the plot. In future applications with larger fields of view, dealing with this technical problem will hopefully become obsolete. The problems mentioned here make it impossible to obtain tighter limits on the cut-off parameter  $s_*$  by including prior knowledge on the velocity dispersion parameter  $\sigma_*$  as it was envisaged in Paper I.

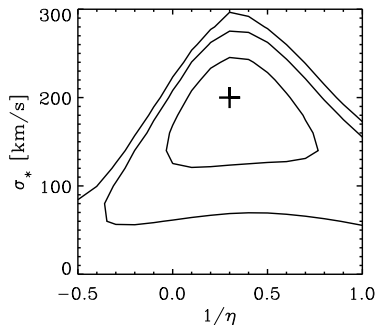


**Figure 9.** Constraints on the scaling parameter  $\eta$  for elliptical cluster galaxies. The plot shows 99.73%, 95.4%, and 68.3% confidence contours for the velocity dispersion  $\sigma_*$  and the scaling index  $\eta$ . Here we assumed a characteristic cut-off radius of  $s_* = 8h^{-1}$  kpc, corresponding to the maximum of the likelihood function in Fig. 7, and a cut-off radius scaling index of  $\nu = 0.5$ . The number of grid points is  $6 \times 6$  and the regularization parameter is  $\lambda = 100$ .

The procedure that had been used by SKSS to determine image ellipticities for the faint objects in the source galaxy catalogue did not include a detailed analysis of instrumental properties as it was carried out by Hoekstra et al. (1997). However, typical distortion values in the field we analysed are considerably larger than their instrumental corrections and so we believe that the implications on our results are negligible.

To obtain the results shown so far we chose  $\eta = 4$  for the index of the scaling law that relates the velocity dispersion parameter of galaxies with different luminosities to those of an  $L_*$ -galaxy. This choice was motivated by the observed Faber-Jackson relation for the velocity dispersion of the stars in elliptical galaxies. If we assume a roughly isothermal mass density profile for the galaxies a similar relation should also hold for the velocity dispersion parameter  $\sigma$  of their dark matter halo. In Fig. 9 we explored the sensitivity of the result to the choice of the scaling index. The figure shows confidence contours in the parameter space defined by the velocity dispersion  $\sigma_*$  and the scaling index  $\eta$ . The value of  $\eta = 4$  lies within the 68% confidence contour and the likelihood difference compared to the maximum of the likelihood function is insignificant. We consider this figure as a necessary check if the information provided by lensing is consistent with our observationally motivated assumptions, and not as a serious attempt to constrain the parameter  $\eta$  from the scarce data available here. For this plot the value for the cut-off radius parameter was fixed at  $s_* = 8h^{-1}$  kpc, which corresponds to the maximum of the likelihood function in Fig. 7. Changing  $s_*$  favours different values for the velocity dispersion parameter and leads to a shift of the contours along the  $\sigma_*$ -coordinate in Fig. 9. However, this does not affect the conclusions regarding the scaling index that we made above. Another parameter whose importance for our results we did not yet discuss is the index  $\nu$  for the cut-off radius scaling law. In contrast to the parameter  $\eta$  we do not have a sound motivation for a particular choice of this index. Changing this parameter between  $\nu = 0$  and  $\nu = 1$  only leads to marginal differences in the likelihood and so it is impossible to achieve limits on this parameter from these

data. In addition, the implications on the appearance of the confidence contours in Figs. 7 to 9, for which  $\nu = 0.5$  was assumed, are very small.

We now turn to a discussion of the absolute likelihood level of our reconstructed solutions. In order to determine the range of values for  $l$  that indicate statistical consistency, we generate random intrinsic ellipticities for the objects in our source galaxy catalogue. Taking the reconstructed solution for the cluster we then calculate their lensed image ellipticities and from that the value of the logarithm of the likelihood. Repeating that procedure for many different intrinsic realizations allows to construct a histogram for  $p(l)$  corresponding to those shown in Fig. 5 for the simulations. As a result we obtain  $l$ -values approximately between 260 and 300. However, the  $6 \times 6$  grid reconstruction without galaxies presented in Fig. 6 only reaches a log-likelihood level of  $l = 138$  for the actually observed image ellipticities, which is far below the value tolerated for an acceptable solution. Including cluster galaxies allows to increase this value by 5 or 6, but refining the cluster grid is much more effective in this respect. The  $12 \times 12$  grid solution also shown in Fig. 6 attains a value as high as  $l = 172$ , which however still falls short of the expected level by a large amount. (The expected level as determined above does not depend very much on the choice for the number of grid points.) In theory the number of grid points and the regularization strength should be adjusted such that consistent likelihood values are reached. This works quite well for our application to simulated observations described in Section 3 where we assumed that the probability density distributions for the intrinsic ellipticity and the redshift of the source galaxies are known. For the application to real data discussed here, however, this is not the case and probably the problem that we face here – and that is reflected by the discrepant log-likelihood levels – is not an inadequate description of the cluster mass distribution, but rather an insufficient knowledge of the properties of the faint galaxies that we have used as lensed sources for our study. In particular we made simple assumptions regarding the redshift distribution and the intrinsic ellipticity distribution of these galaxies. In practice these could be quite different for galaxies of different magnitude, surface brightness or morphology. In order to use a check of the absolute likelihood level as a powerful tool for evaluating the reliability of our description of the cluster mass distribution, a detailed understanding of the source galaxy population is warranted.

## 5 DISCUSSION

Continuing our discussion of Paper I we investigated methods to constrain the mass distribution of cluster galaxies by weak lensing. In Paper I we concluded that a comprehensive method should simultaneously take into account the lensing effects of individual cluster galaxies as well as those of a general cluster component. To this end we developed a regularized cluster lens reconstruction algorithm that directly uses the image ellipticities of individual background galaxies as observables, and that allows to explicitly include the presence of cluster galaxies in the analysis. We parametrize the mass distribution of cluster galaxies by truncated isothermal spheres and apply simple scaling laws to relate the halo

properties to those of  $L_*$ -galaxies according to the galaxy luminosity. For each value of the galaxy parameters – velocity dispersion  $\sigma_*$  and cut-off radius  $s_*$  of an  $L_*$ -galaxy – the method allows to determine the best representation for the underlying cluster mass component that is consistent with the observed image ellipticities. We tested the method on simulations and achieved convincing and robust results. If the dark matter distribution around cluster galaxies is rather extended, it is not straightforward to make a clear-cut distinction between mass belonging to a global cluster component or to galaxy haloes. An important result from these simulations is that the distance between the grid points of the cluster component determines the scale for a somewhat artificial separation of the mass located in galaxies and the mass attributed to the global cluster component.

We applied our method to a WFPC2 image of the galaxy cluster Cl0939+4713. Our reconstruction of the cluster mass distribution is consistent with the result of SKSS who used the same object catalogue but a different reconstruction technique. However, the robustness of the result should finally be verified by using observations with a larger field of view. This would also allow to break the mass sheet degeneracy that prevents us from deriving absolute mass estimates here. In this respect another factor of uncertainty is the unknown redshift distribution of the source galaxies.

The galaxy-galaxy lensing analysis provided a significant detection (approximately at the 99% to 99.9% confidence level) of the lensing effects induced by luminous elliptical cluster galaxies. In fact it had already been speculated by Dressler et al. (1994b) that some of the arclets in this WFPC2 image ‘appear to be background sources lensed by individual galaxies rather than the overall cluster potential’. The likelihood function attains its maximum at rather low values for the cut-off radius parameter. However, the small number of lens galaxies included in our study does not allow to derive strong limits for the parameters describing the galaxy haloes. Changing the assumptions that we were obliged to make regarding the mass sheet degeneracy and the redshift distribution of the sources leads to a rescaling of the galaxy-galaxy lensing result. For this reason we do not quote galaxy mass-to-light ratios or values for the fraction of the total mass bound to galaxies in this paper. Our result is consistent with the result of Natarajan et al. (1997) who applied the methods of Natarajan & Kneib (1997) to analyse a mosaic of WFPC2 images of the cluster AC114. However, significant differences of their approach compared to ours make a quantitative comparison of the results difficult.

We consider the application to Cl0939+4713 described in this paper as a successful test of our maximum likelihood technique for galaxy-galaxy lensing in clusters of galaxies. The problems we encountered are not inherent to our method and mainly resulted from the small size of the image we analysed. Ideal observations for this project should include deep exposures with high image quality and large fields of view, which would make it feasible to test possible variations of the halo properties with the density of the environment. Another important ingredient should be supplementary imaging in different colours in order to assure a reliable selection of cluster galaxies and potentially for deriving photometric redshift estimates for the galaxies used as sources. The benefit of photometric redshift information for galaxy-galaxy lensing studies (in the field) was empha-

sized by Schneider & Rix (1997) and has been demonstrated by Hudson et al. (1997) in their analysis of the *Hubble Deep Field*. Making use of available redshift information for individual source galaxies also allows us to reduce the noise in cluster reconstructions. [In our implementation the approximation (7) for the probability density distribution of image ellipticities can then be replaced by the simpler expression (6).] This was also recognized by Seljak (1997) in a similar context.

The analysis of the kind of observational data sets envisaged above, which are most likely to be available within the next few years, will provide the opportunity to compare the lensing constraints to recent numerical studies of the properties of galaxy haloes within clusters (Tormen, Diaferio & Syer 1997, Ghigna et al. 1998). In addition, a comparison and combination of the galaxy-galaxy lensing results with morphological studies of the galaxy population in these clusters (e.g. Oemler, Dressler & Butcher 1997) could help to obtain observational evidence for the physical processes [such as the ‘galaxy harassment’ picture suggested by Moore et al. (1996)] that might be responsible for the evolution of cluster galaxies.

## ACKNOWLEDGMENTS

We thank Simon White for carefully reading the manuscript. This work was supported in part by the Deutscher Akademischer Austauschdienst (Doktorandenstipendium HSP III), the Sonderforschungsbereich 375-95 der Deutschen Forschungsgemeinschaft and the TMR Network on Research in Gravitational Lensing.

## REFERENCES

- Bartelmann M., Narayan R., Seitz S., Schneider P., 1996, *ApJ*, 464, L115  
 Belloni P., Bruzual A.G., Thimm G.J., Röser H.-J., 1995, *A&A*, 297, 61  
 Brainerd T.G., Blandford R.D., Smail I., 1996, *ApJ*, 466, 623  
 Bridle S.L., Hobson M.P., Lasenby A.N., Saunders R., 1998, preprint, astro-ph/9802159  
 Dell’Antonio I.P., Tyson J.A., 1996, *ApJ*, 473, L17  
 Dressler A., Gunn J.E., 1992, *ApJS*, 78, 1  
 Dressler A., Oemler A., Butcher H.R., Gunn J.E., 1994a, *ApJ*, 430, 107  
 Dressler A., Oemler A., Sparks W.B., Lucas R.A., 1994b, *ApJ*, 435, L23  
 Geiger B., Schneider P., 1998, *MNRAS*, 295, 497, (Paper I)  
 Ghigna S., Moore B., Governato F., Lake G., Quinn T., Stadel J., 1998, preprint, astro-ph/9801192  
 Griffiths R.E., Casertano S., Im M., Ratnatunga K.U., 1996, *MNRAS*, 282, 1159  
 Hoekstra H., Franx M., Kuijken K., Squires G., 1997, preprint, astro-ph/9711096  
 Hudson M.J., Gwyn S.D.J., Dahle H., Kaiser N., 1997, preprint, astro-ph/9711341  
 Moore B., Katz N., Lake G., Dressler A., Oemler A., 1996, *Nat*, 379, 613  
 Narayan R., Nityananda R., 1986, *ARA&A*, 24, 127  
 Natarajan P., Kneib J.-P., 1997, *MNRAS*, 287, 833  
 Natarajan P., Kneib J.-P., Smail I., Ellis R.S., 1997, preprint, astro-ph/9706129  
 Oemler A., Dressler A., Butcher H.R., 1997, *ApJ*, 474, 561

- Press W.H., Teukolsky S.A., Vetterling W.T., Flannery B.P., 1992, Numerical Recipes in FORTRAN. Cambridge University Press, Cambridge
- Schneider P., Rix H.-W., 1997, ApJ, 474, 25
- Seitz S., Schneider P., 1996, A&A, 305, 383
- Seitz C., Schneider P., 1997, A&A, 318, 687
- Seitz S., Schneider P., Bartelmann M., 1998, preprint, astro-ph/9803038
- Seitz C., Kneib J.-P., Schneider P., Seitz S., 1996, A&A, 314, 707, (SKSS)
- Seljak U., 1997, preprint, astro-ph/9711124
- Smail I., Dressler A., Couch W.J., Ellis R.E., Oemler A., Butcher H., Sharples R.M., 1997, ApJS, 110, 213
- Squires G., Kaiser N., 1996, ApJ, 473, 73
- Tormen G., Diaferio A., Syer D., 1997, preprint, astro-ph/9712222
- Trager S.C., Faber S.M., Dressler A., Oemler A., 1997, ApJ, 485, 92
- Tyson J.A., Valdes F., Jarvis J.F., Mills A.P., 1984, ApJ, 281, L59

## APPENDIX A:

In this appendix we prove a statement given in Section 2.2 concerning the dispersion of the probability density distribution for the image ellipticity of lensed background galaxies. Seitz & Schneider (1997) showed that the moments of the complex ellipticity parameter  $\epsilon$  can be expressed in terms of the reduced shear:

$$\langle \epsilon^n \rangle_{\epsilon_s} = g^n \quad \text{for } |g| \leq 1. \quad (\text{A1})$$

In the following we perform a rotation of the ellipticity coordinates such that the imaginary component of the (reduced) shear vanishes, i.e., we transform  $g$  and  $\epsilon$  into ‘local shear coordinates’. This can be expressed as

$$\tilde{g} := \frac{\gamma^*}{|\gamma|} g = \frac{|\gamma|}{1-\kappa} \quad \text{and} \quad \tilde{\epsilon} = \tilde{\epsilon}_1 + i\tilde{\epsilon}_2 := \frac{\gamma^*}{|\gamma|} \epsilon.$$

We calculate the expectation value of  $\tilde{\epsilon}^2 = \tilde{\epsilon}_1^2 - \tilde{\epsilon}_2^2 + 2\tilde{\epsilon}_1\tilde{\epsilon}_2 i$  by applying equation (A1):

$$\langle \tilde{\epsilon}^2 \rangle_{\epsilon_s} = \langle \tilde{\epsilon}_1^2 \rangle_{\epsilon_s} - \langle \tilde{\epsilon}_2^2 \rangle_{\epsilon_s} + 2\langle \tilde{\epsilon}_1 \tilde{\epsilon}_2 \rangle_{\epsilon_s} i = \tilde{g}^2. \quad (\text{A2})$$

The quantity  $\tilde{g}$  is real and so it follows from this equation that  $\langle \tilde{\epsilon}_1 \tilde{\epsilon}_2 \rangle_{\epsilon_s} = 0$ . Now we can express the variance of  $\tilde{\epsilon}_1$  as

$$\sigma_{\tilde{\epsilon}_1}^2 := \langle \tilde{\epsilon}_1^2 \rangle_{\epsilon_s} - \langle \tilde{\epsilon}_1 \rangle_{\epsilon_s}^2 = \langle \tilde{\epsilon}_1^2 \rangle_{\epsilon_s} - \tilde{g}^2 = \sigma_{\tilde{\epsilon}_2}^2.$$

In the first equality we used equation (A1) and the second follows from equation (A2) with the definition of  $\sigma_{\tilde{\epsilon}_2}^2 := \langle \tilde{\epsilon}_2^2 \rangle_{\epsilon_s} - \langle \tilde{\epsilon}_2 \rangle_{\epsilon_s}^2$  and  $\langle \tilde{\epsilon}_2 \rangle_{\epsilon_s} = 0$  which again follows from (A1). Thus the dispersion of the probability density distribution in local shear direction is equal to the dispersion in the perpendicular direction:  $\sigma_{\tilde{\epsilon}_1} = \sigma_{\tilde{\epsilon}_2}$ . For  $|g| > 1$  this result can be derived analogously.

## APPENDIX B:

This appendix gives the expressions needed to calculate the derivatives of  $\hat{l}$  with respect to the potential values on the grid points. The derivative of the logarithm of the probability density can be written as

$$\frac{\partial \ln p_\epsilon(\epsilon)}{\partial \psi_{\alpha\beta}} = \frac{\partial \ln p_\epsilon(\epsilon)}{\partial \kappa_\infty} \frac{\partial \kappa_\infty}{\partial \psi_{\alpha\beta}}$$

$$+ \left[ \frac{\partial \ln p_\epsilon(\epsilon)}{\partial |\gamma_\infty|} \frac{\gamma_{1\infty}}{|\gamma_\infty|} - \frac{\partial \ln p_\epsilon(\epsilon)}{\partial \phi_\gamma} \frac{\gamma_{2\infty}}{|\gamma_\infty|^2} \right] \frac{\partial \gamma_{1\infty}}{\partial \psi_{\alpha\beta}} + \left[ \frac{\partial \ln p_\epsilon(\epsilon)}{\partial |\gamma_\infty|} \frac{\gamma_{2\infty}}{|\gamma_\infty|} + \frac{\partial \ln p_\epsilon(\epsilon)}{\partial \phi_\gamma} \frac{\gamma_{1\infty}}{|\gamma_\infty|^2} \right] \frac{\partial \gamma_{2\infty}}{\partial \psi_{\alpha\beta}}.$$

The symbol  $\phi_\gamma$  represents the phase of the complex shear parameter  $\gamma_\infty = |\gamma_\infty| e^{i\phi_\gamma}$ . The derivative of  $\ln p_\epsilon(\epsilon)$  with respect to  $\kappa_\infty$  is given by

$$\begin{aligned} \frac{\partial \ln p_\epsilon(\epsilon)}{\partial \kappa_\infty} &= \frac{\tilde{\epsilon}_1 - \tilde{g}_r}{\sigma_{\tilde{\epsilon}_1}^3(\tilde{g}_r)} \left[ \frac{\partial \tilde{g}_r}{\partial \kappa_\infty} \sigma_{\tilde{\epsilon}_1}(\tilde{g}_r) + (\tilde{\epsilon}_1 - \tilde{g}_r) \frac{\partial \sigma_{\tilde{\epsilon}_1}(\tilde{g}_r)}{\partial \kappa_\infty} \right] \\ &+ \frac{\tilde{\epsilon}_2^2}{\sigma_{\tilde{\epsilon}_2}^3(\tilde{g}_r)} \frac{\partial \sigma_{\tilde{\epsilon}_2}(\tilde{g}_r)}{\partial \kappa_\infty} \\ &- \frac{1}{\sigma_{\tilde{\epsilon}_1}(\tilde{g}_r)} \frac{\partial \sigma_{\tilde{\epsilon}_1}(\tilde{g}_r)}{\partial \kappa_\infty} - \frac{1}{\sigma_{\tilde{\epsilon}_2}(\tilde{g}_r)} \frac{\partial \sigma_{\tilde{\epsilon}_2}(\tilde{g}_r)}{\partial \kappa_\infty}, \end{aligned}$$

a similar expression holds for  $\partial \ln p_\epsilon(\epsilon)/\partial |\gamma_\infty|$ , and the derivative with respect to  $\phi_\gamma$  is

$$\frac{\partial \ln p_\epsilon(\epsilon)}{\partial \phi_\gamma} = -\frac{(\tilde{\epsilon}_1 - \tilde{g}_r) \tilde{\epsilon}_2}{\sigma_{\tilde{\epsilon}_1}^2} + \frac{\tilde{\epsilon}_2 \tilde{\epsilon}_1}{\sigma_{\tilde{\epsilon}_2}^2}.$$

The derivatives remaining in these formulae are trivial to calculate from the definitions of the respective quantities. The derivative of the term that ensures the correct total mass reads

$$\begin{aligned} \frac{\partial \ln p_{\bar{\kappa}_C}}{\partial \psi_{\alpha\beta}} &= \sum_{\gamma, \delta=1}^n \frac{\partial \ln p_{\bar{\kappa}_C}}{\partial \kappa_{C\gamma\delta}} \frac{\partial \kappa_{C\gamma\delta}}{\partial \psi_{\alpha\beta}} \\ &= -\frac{\bar{\kappa}_C - f_C \bar{\kappa}_\infty}{\sigma_{\bar{\kappa}_C}^2} \frac{1}{n^2} \sum_{\gamma, \delta=1}^n \frac{\partial \kappa_{C\gamma\delta}}{\partial \psi_{\alpha\beta}}, \end{aligned}$$

and the entropy term yields

$$\frac{\partial S}{\partial \psi_{\alpha\beta}} = \sum_{\gamma, \delta=1}^n \frac{\partial S}{\partial \kappa_{C\gamma\delta}} \frac{\partial \kappa_{C\gamma\delta}}{\partial \psi_{\alpha\beta}} = \sum_{\gamma, \delta=1}^n \sum_{\epsilon, \zeta=1}^n \frac{\partial S}{\partial \hat{\kappa}_{C\epsilon\zeta}} \frac{\partial \hat{\kappa}_{C\epsilon\zeta}}{\partial \kappa_{C\gamma\delta}} \frac{\partial \kappa_{C\gamma\delta}}{\partial \psi_{\alpha\beta}}$$

with

$$\frac{\partial \hat{\kappa}_{C\epsilon\zeta}}{\partial \kappa_{C\gamma\delta}} = \frac{1}{\kappa_{P\epsilon\zeta}} \left( \frac{\delta_{\gamma\epsilon} \delta_{\delta\zeta} - \hat{\kappa}_{C\epsilon\zeta}}{\sum_{\eta, \theta=1}^n \hat{\kappa}_{C\eta\theta}} \right) \quad \text{and} \quad \frac{\partial S}{\partial \hat{\kappa}_{C\epsilon\zeta}} = \frac{1}{\hat{\kappa}_{C\epsilon\zeta}}.$$

Although these expressions look rather complicated they can be conveniently implemented technically and do not cause major computational problems.